Steric shielding protected and acidity-activated pop-up of ligand for tumor enhanced photodynamic therapy

Kai Han[a,b,**], Zhaoyu Ma[a], Xinxin Dai[a,b], Jin Zhang[a], Heyou Han[a,*]

[a] State Key Laboratory of Agricultural Microbiology, College of Science, Huazhong Agricultural University, Wuhan 430070, China
[b] Bio-Medical Center of Huazhong Agricultural University, Wuhan 430070, China

ABSTRACT

Tumor targeted drug delivery *in vivo* remains a significant challenge in tumor therapy. In this article, we fabricated a steric shielding protected/tumor acidity-activated chimeric peptide for tumor targeted photodynamic therapy. This amphiphilic chimeric peptide could form spherical nanoparticles at neutrally physiological environment with the shielding of biotin molecule (tumor target ligand). When in tumor acidic microenvironment, acidity-sensitive dimethylmaleic amide was rapidly hydrolyzed, resulting in subsequent liberation of $(Lys)_8$ and the recovery of intramolecular electrostatic interaction between $(Lys)_8$ and $(Glu)_8$. Then $(Glu)_8$ folded $(Lys)_8$ and biotin molecule was popped up to the surface of nanoparticles. Both *in vitro* and *in vivo* studies indicated that this steric shielding protected/tumor acidity-activated pop-up strategy demonstrated here could remarkably enhance tumor specific accumulation/internalization of chimeric peptide, improve photodynamic therapy efficacy and minimize the side effects. This strategy should not only be used for phototherapy, but also open a window to endow nanocarriers with effective tumor target ability.

1. Introduction

Fabrication of novel nanocarriers to enhance therapeutic efficacy of drugs has attracted considerable attention over the past decades [1–6]. Despite the remarkable progress in nanocarriers, site-specific delivery of drugs to tumor remains a great challenge [7–12]. The most commonly used strategy to realize tumor target is the direct surface modification of nanocarriers with targeting ligands including monoclonal antibodies or peptides [13,14]. These ligands can bind receptors on cell membrane, accelerate nanocarriers across cell barriers and improve drug accumulation in tumor. However, normal tissues also expressed certain receptors. Non-specific interaction between ligand modified nanocarriers and normal tissues decreases the targeted therapeutic efficacy during *in vivo* circulation [15]. To overcome this dilemma, the concept of shielding protected/stimuli-activation strategy has been proposed recently [16–18]. Generally, targeting moieties are shielded by photo-responsive cages or long-chain PEG to avoid the contact with normal tissue. Once arriving at tumor region, shield groups in nanocarriers can be detached under internal/external stimuli including UV light or enzymes. Then the exposed targeting moieties mediate accelerated cellular internalization. Unfortunately, detachment of shielding groups is always severely retarded, partly because of the

insufficient enzyme concentration or poor penetration depth of UV light. On the other hand, many enzymes only exist in some specific tumor types, which restrict the application of nanocarriers. Thus, construction of highly sensitive nanocarriers with broad-spectrum tumor target is still desirable and highly challenging.

It is known that extracellular pH slightly decreases in almost all solid tumors [19,20]. Meanwhile, the pH scale is relatively narrow, which ensures sufficient pH sensitivity. Motivated by these merits, some pioneering studies have developed intelligent pH responsive nanocarriers featuring shielding protected/stimuli-activation property [21–25]. One of the most typical examples is charge-reversal nanocarriers reported by Wang and co-workers. Negatively charged nanocarriers are shielded by maleic anhydride derivatives and become positively charged in tumor acidity, which promotes intracellular uptake of gene or drugs [26–28]. Note that the enhanced cellular uptake of most pH responsive nanocarriers is largely based on non-specific electrostatic interaction between acidity-activated cationic moieties and negatively charged cell membrane. However, the high pH sensitivity is always accompanied with potential physiological instability of nanocarriers to some extent. This issue will compromise the target ability inevitably.

Herein, we designed a steric shielding protected chimeric peptide
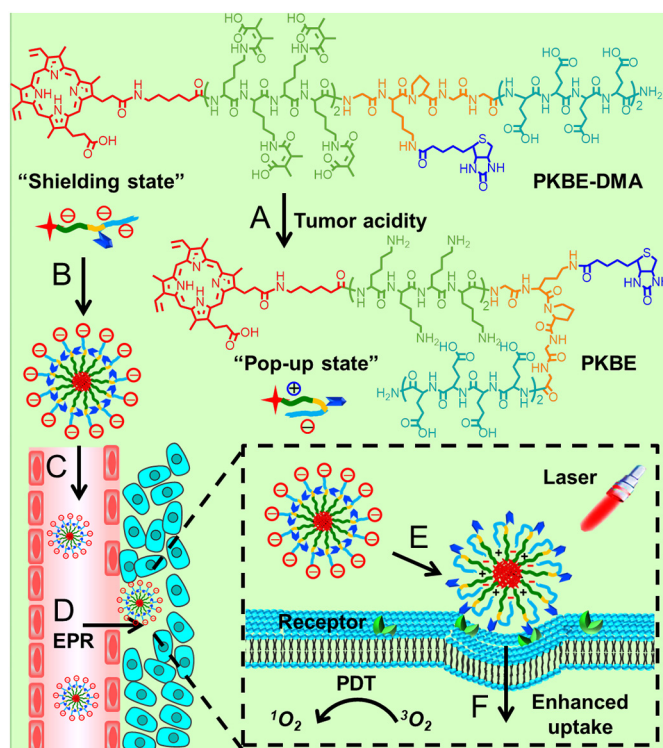
Scheme 1. Schematic illustration of steric shielding and acidity-activated pop-up of ligand for tumor selective PDT. (A) Chemical structure of PKBE-DMA and tumor acidity-activated DMA detachment and biotin exposure. (B) PBKE-DMA self-assembled into spherical nanoparticles and (C) *in vivo* injected; (D) tumor specific accumulation of PKBE-DMA in tumor *via* enhanced penetration and retention (EPR) effect; (E) tumor acidity-activated DMA detachment and electrostatic interaction mediated biotin exposure; (F) receptor mediated enhanced cellular uptake and PDT under light irradiation.

for tumor acidity-activated pop-up of targeting ligand for enhanced photodynamic therapy. This chimeric peptide employed an alkylated photosensitizer protoporphyrin IX (PpIX) as the hydrophobic core, while hydrophilic shell was composed of dimethylmaleic anhydride (DMA) modified (Lys)$_8$ and (Glu)$_8$ using Gly-Lys(biotin)-Pro-Gly-Gly as a linker (K$_8$GK(Biotin)PGGE$_8$). The obtained chimeric peptide was designated as PKBE-DMA. As shown in Scheme 1, PKBE-DMA could self-assemble into spherical nanoparticles and resist protein adsorption at neutrally physiological condition, while the biotin ligand was shielded in hydrophilic shell due to the strong electrostatic repulsion among negatively charged carboxylic groups. Once arriving at mildly acidic tumor environment, DMA groups were rapidly detached and amine residuals of Lys were liberated. Because of the existence of proline and the flexibility of GKPGG linker, a zipper-like fold would form assisted by the electrostatic attraction between (Lys)$_8$ and (Glu)$_8$ [29,30]. This fold could effectively avoid the non-specific interaction between (Lys)$_8$ and cell membrane. Importantly, it exposed the targeting biotin molecule, which further realized selective accumulation/internalization and photodynamic therapeutic efficacy of chimeric peptide in tumor region.

2. Materials and methods

2.1. Chemicals

N-fluorenyl-9-methoxycarbonyl (Fmoc)-protected L-amino acids, diisopropylethylamine (DiEA), piperidine, Rink-NH$_2$ resin, trifluoroacetic acid (TFA), o-benzotriazole-*N,N,N′,N′*-tetramethyluroniumhexafluorophosphate (HBTU) and triisopropylsilane (TIS) were purchased from GL Biochem Ltd. (China). fluorescamine, PpIX, succinic anhydride and DMA were obtained from Aladdin

Reagent Chemical Co. (China). Fetal bovine serum (FBS), Dulbecco's modified Eagle's medium (DMEM), MTT, trypsin and penicillin-streptomycin were purchased from GIBCO Invitrogen Corp. All other reagents were used without further purification.

2.2. Synthesis of PKBE and PKE

Both PKBE and PKE were conjugated on Rink-NH$_2$ resin *via* a typical SPPS method [31,32]. During the synthesis, 20% piperidine/DMF (*v*/*v*) was employed to cleave the protective Fmoc group while HBTU/DiEA was used to catalyze coupling of amino acids. To introduce biotin molecule at the side chain of chimeric peptide, Fmoc-Lys(Mtt)-COOH peptide was used and Mtt group was removed by 1% TFA/DCM for 45 min (10 × 5 min). Chimeric peptide was cleaved from Rink-NH$_2$ resin in the presence of TFA, H$_2$O and TIS (volume ratio: 95:2.5:2.5) for 1.5 h. Then peptide was precipitated in diethyl ether and collected by centrifugation. Peptide was dried under vacuum overnight and then dissolved in distilled water for freeze-drying. Peptide was purified by high performance liquid chromatography (HPLC) and the molecular weight was determined *via* electrospray ionization mass spectrometry (ESI-MS). Multi-charged peaks at 848 ($[M + 4H + 3TFA]^{4+}$) and 1694 ($[M + 2H + 3TFA]^{2+}$) were found in PKE, and the purity was over > 90% (Fig. S1).

2.3. Synthesis of PKBE-DMA

PKBE (20 mg) and DMA (7.8 mg, 4 equiv. to amino group) were dissolved in NaOH solution and the final pH kept around 10. The solution was stirred in dark for 24 h. Then free DMA was removed *via* dialysis method in NaOH solution. PKBE-DMA was obtained *via* freeze-drying. PpIX-Ahx-K$_8$(DMA)-GKPGGE$_8$ (denoted as PKE-DMA) and succinic amide modified PpIX-Ahx-K$_8$-GK(Biotin)PGGE$_8$ (denoted as PKBE-SA) were prepared *via* the similar method [33].

2.4. Characterization of PKBE-DMA

UV–vis spectrum of PKBE-DMA was recorded *via* UV–vis spectrophotometer. Zeta potential of PKBE-DMA (50 mg/L) at pHs of 6.8 and 7.4 were determined *via* Nano-ZS ZEN3600 (Malvern Instruments). PKBE-DMA was incubated in PBS buffer at pHs of 6.8 and 7.4 for 4 h, and then transmission electron microscopy (TEM, JEM-2100 microscope) was employed to observe the morphology of PKBE-DMA (50 mg/L) at pHs of 6.8 and 7.4. PKBE-SA and PKE-DMA were used as controls. Fluorescence of PKBE-DMA, PKBE-SA and PKE-DMA was measured *via* a fluorospectrophotometer.

2.5. Critical micelle concentration (CMC) measurement

The CMC value of PKBE-DMA at pHs of 6.8 and 7.4 was determined by fluorescence spectroscopy. Pyrene was the fluorescent probe. Briefly, various peptide solutions containing 6×10^{-7} M pyrene was prepared in PBS buffer (pH 6.8 or 7.4). Fluorescence spectra were recorded on a LS55 luminescence spectrometer (Perkin-Elmer). Emission was 390 nm and excitation spectra ranged from 300 to 360 nm. The change of the intensity ratio of the third and first vibronic bands (I_3/I_1) was plotted against the logarithm of the peptide concentrations to detect CMC.

2.6. Reactive oxygen species (ROS) determination

ROS generation was detected as our previous work [34]. Briefly, 2′,7′-dichlorodihydrofluorescein diacetate (DCFH-DA, 30 μL, 1 mg/mL), PKBE-DMA (50 μL, 1 mg/mL) and DI water (920 μL) were mixed. Then the solution received 630 nm light irradiation with preset times. The fluorescence spectrum of DCF was immediately recorded *via* fluorescence spectrophotometer (excitation wavelength: 485 nm), and the fluorescence intensity was denoted as F_t. The ROS generation was

defined as F_t/F_0, in which F_0 was the initial fluorescence of NaOH pretreated DCFH-DA alone. PpIX (in 0.05% DMSO) was employed as a control.

2.7. DMA detachment test of PKBE-DMA

PKBE-DMA (50 mg/L) was pre-incubated in PBS buffer at pH 6.8 or 7.4 for preset times (0–120 min), respectively. Subsequently, fluorescamine solution (2 mg/mL in DMF) was added to these samples. After incubation in dark for 10 min, fluorescence spectrum at preset times was recorded *via* fluorospectrophotometer. The excitation wavelength was 365 nm while emission wavelength at 475 nm was defined as F_t. The degradation of DMA was calculated based on the following formula: $(F_t - F_b)/(F_0 - F_b) \times 100\%$, F_b and F_0 was the fluorescence emission intensity at 475 nm of PBS and the sample at 0 min, respectively. The data was the average value of three independent measurements.

2.8. HABA/avidin assay

Hydroxyazobenzene-2-carboxylic acid (HABA, 24.2 mg) was dissolved in NaOH solution (10 mL). Meanwhile, 2.0 mg avidin was dissolved in 1.94 mL of 50 mM PBS (pH 6.8 or 7.4) with 50 mM NaCl. Thereafter, 60 μL of HABA solution was added to the avidin solution to obtain the HABA/avidin solution (pH 6.8 or 7.4). The UV–vis intensity of HABA/avidin solution at 500 nm was recorded. PKBE-DMA solution was incubated in PBS buffer (pH 6.8 and 7.4) for 0.5 h and 2 h, respectively. Then 675 μL of HABA/avidin solution (pH 6.8 or 7.4) was mixed with 75 μL of PKBE-DMA solution for 0.5 h. Since the higher affinity for avidin, the exposed biotin could displace HABA from its interaction with avidin. The absorbance at 500 nm would decrease proportionately, which was detected *via* UV–vis spectrum.

2.9. Circular dichroism (CD) spectrum

50 mg/L PKBE-DMA was incubated in PBS buffer (pH 6.8 or 7.4) for 2 h. Then the CD spectrum was recorded on a J-1500 spectropolarimeter (Jasco, Japan). The spectra were scanned from 240 to 190 nm. Quartz cell was used throughout. The data was recorded for three times.

2.10. In vitro cellular uptake observation

SCC-7 (squamous cell carcinoma), HeLa (Human cervical cancer cells) and COS7 (African green monkey SV40-transfected kidney fibroblast cells) cells were seeded in 6-well plates, respectively. At the 24 h post incubation, the cultural medium was replaced with various samples including PKBE-DMA (105 mg/L), PKBE-SA and PKE-DMA in fresh medium (pH 6.8 or 7.4), respectively. The content of PpIX was equivalent. At 4 h post incubation, samples were removed and cells were thoroughly washed with PBS buffer. Then samples were directly observed *via* confocal laser scanning microscopy (CLSM) and the excitation wavelength was 405 nm for PpIX.

2.11. In vitro cytotoxicity evaluation

In vitro cytotoxicity of PKBE-DMA, PKE-DMA and PKBE-SA against SCC-7, HeLa and COS7 cells were measured *via* MTT assay. Cells were incubated on 96-well plates for 24 h. Subsequently, the cultural medium was removed, followed by adding various concentrations of PKBE-DMA, PKBE-SA and PKE-DMA in 10% FBS at pH 6.8 or 7.4. At 4 h post incubation, the samples were replaced with 200 μL 10% FBS. Thereafter, cells received 630 nm light irradiation for 45 s (10 mW/cm^2). Cells were further incubated for 48 h. Subsequently, 20 μL MTT (5 mg/mL) was added to each well. The supernatant was replaced with DMSO (150 μL) at 4 h post incubation. A microplate reader (Bio-Rad, Model 550, USA) was used to read the optical density (OD) of every well at 490 nm. The relative cell viability was calculated based on the formula: cell viability (%) = OD$_{(sample)}$/OD$_{(control)}$ × 100%. OD$_{(sample)}$ and OD$_{(control)}$ were the OD values in the presence or absence of sample, respectively.

2.12. In vivo fluorescence imaging and tissue distribution study

SCC-7 cells (5×10^6 cells per mouse) were subcutaneous injected into the back of female BABL/c nude mice. 12 days later, the volume of SCC-7 tumor xenograft reached around 50 mm^3. PKBE-SA, PKE-DMA and PKBE-DMA were injected into SCC-7 tumor-bearing mice through tail vein, respectively. The equivalent PpIX dosage of each formulation was 3 mg/kg. At the preset times, mice were anesthetized and put on a small animal imaging system in Institute of Virology (Wuhan, Chinese Academy of Sciences). Fluorescence imaging was recorded using a Green channel. At 24 h post injection, mice were sacrificed and the organs including heart, liver, spleen, lung, kidney and tumor were exfoliated. These samples were washed with PBS and then imaged directly. To compare the fluorescence intensity of various samples in tumor *via* CLSM, the tumor was exfoliated at the 6th h and the frozen sections were observed immediately. PpIX was excited with 405 nm laser while the emission range was from 590 nm to 650 nm. Besides, the frozen sections of tumor tissue was stained with DCFH-DA for 20 min, then the sample was washed with PBS and the green fluorescence was observed to evaluate the ROS generation *via* CLSM.

2.13. Pharmacokinetics in vivo

Samples were intravenously injected into SCC-7 tumor-bearing nude mice through tail vein. The equivalent PpIX dosages of each formulation were 2.5 mg/kg. Mice blood was collected at preset times. And these blood samples were diluted with PBS buffer. Then the samples were freeze-thawed repeatedly. Thereafter, cells were under ultrasound, fluorospectrophotometer was employed to record the fluorescence intensity of PpIX in various samples.

2.14. In vivo antitumor test

SCC-7 tumor-bearing mice with tumor size around 50 mm^3 were divided into 5 groups randomly. Each group had 4 mice. The mice were intravenously injected with PBS buffer, PKBE-SA, PKE-DMA and PKBE-DMA every day, respectively. The concentration of PpIX was 3 mg/kg mouse body weight. At the 6 h post *in vivo* injection, the group of PKBE-SA, PKE-DMA and PKBE-DMA received 10-min light irradiation (laser wavelength 638 nm, power density: 0.2 W/cm^2). Meanwhile, PBS group and another PKBE-DMA group did not receive light irradiation. The length (L) and width (W) of tumor and body weight of all mice were recorded every day. Tumor volume was calculated as following: $L \times W^2/2$.

2.15. In vivo systemic toxicity evaluation

Mice blood of various groups was obtained from eyes after the treatment was finished. These blood samples were solidified at room temperature for 1.5 h and then centrifuged for 5 min to get serum samples. The biological indexes of GPT, AST, UA, BUN, A/G and CK in serum samples were determined at Union Hospital (Wuhan, China). The data were mean of three replicates. Thereafter, mice were sacrificed and the organs of heart, liver, spleen, lung, kidneys and tumor were collected. These organs and tumors were incubated in 4% formalin and then embedded in paraffin for hematoxylin and eosin (H&E) staining.

2.16. Statistical analysis

Student's *t*-test was employed to evaluate the statistical analysis.
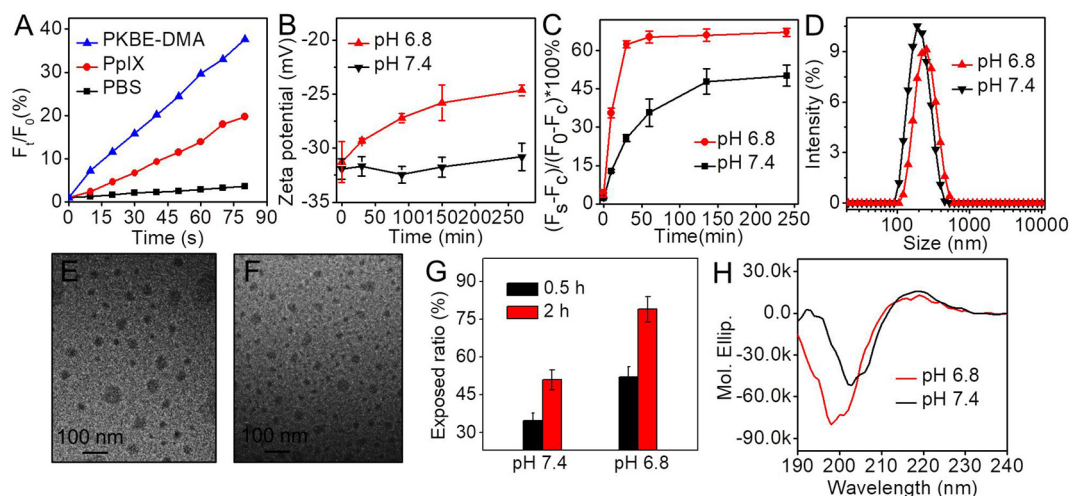
Fig. 1. Characterization. (A) ROS measurement of PKBE-DMA, and PpIX in 0.05% DMSO was used as a control. (B) Zeta potential of PKBE-DMA at pHs of 6.8 and 7.4 at different incubation times. (C) DMA detachment of PKBE-DMA at pHs of 6.8 and 7.4 and fluorescamine was used as a sensor. (D) Hydrodynamic sizes of PKBE-DMA in PBS buffer at pHs of 6.8 and 7.4. TEM images of PKBE-DMA at pHs of (E) 6.8 and (F) 7.4. (G) Exposed biotin ratio when PKBE-DMA was incubated at pHs of 6.8 and 7.4 for 0.5 h and 2 h. (H) CD spectrum of PKBE-DMA at pHs of 6.8 and 7.4. The concentration of PKBE-DMA was 50 mg/L.

$p < 0.05$ means the statistical significant differences between different groups.

3. Results and discussion

3.1. Synthesis and characterizations of PKBE-DMA

Amphiphilic PpIX-Ahx-K_8-GK(Biotin)PGGE_8 (denoted as PKBE) was synthesized *via* standard Fmoc solid phase peptide synthesis (SPPS) method (Scheme S1). The theoretical molecular weight of PKBE was 3351.7. ESI-MS (Fig. S2A) revealed that multi-charged peaks at 952.9 ($[M + 4H + 4TFA]^{4+}$) and 598.9 ($[M + 6H + 2TFA]^{6+}$) were found, suggesting the validity of PKBE. And the purity (> 90%) was verified by HPLC (Fig. S2B). Subsequently, PKBE was reacted with DMA at alkaline solution and then purified *via* a dialysis method to get pH sensitive PKBE-DMA. PKBE-DMA exhibited well water solubility, and UV–vis spectrum demonstrated that negligible π-π stacking existed among PpIX molecules according to the appearance of a sharp Soret band around 400 nm (Fig. S3) [35,36]. Fig. 1A indicated that the fluorescence intensity of dichlorofluorescein increased rapidly with prolonging of irradiation time, when PKBE-DMA was incubated with ROS sensor DCFH-DA. In contrast, the fluorescence intensity increment in PpIX group is significantly retarded. Apparently, PKBE-DMA with well water solubility could reduce the aggregation and self-quenching of PpIX, which would benefit the generation of ROS [37–39].

To verify the acidic responsiveness of PKBE-DMA, the zeta potential change as a function of time was recorded. pH 6.8 was chosen to simulate tumor acidic environment. As shown in Fig. 1B, zeta potential of PKBE-DMA at pH 7.4 was relatively stable, while at pH 6.8 the zeta potential gradually increased with prolonging of incubation time. Clearly, dimethylmaleic amide between Lys and DMA could be hydrolyzed rapidly at acidic environment, since the nearby free carboxylic acid in DMA would attack the dimethylmaleic amide with the help of H^+, leading to the intramolecular catalysis as well as the detachment of DMA [25–27]. The detachment of DMA group liberated amine residual of Lys, leading to the increase of zeta potential. For comparison, PKBE-SA exhibited pH insensitivity, whose zeta potentials always kept at around −28 mV at pHs of 6.8 and 7.4 with prolonging of incubation time (Fig. S4). It was due to fact that the conformation of succinic amide in PKBE-SA was flexible. The terminal carboxyl group was far away from amide group, which could not assist the hydrolysis of succinic amide. As a result, succinic amide was relative stable under mild

acidity [40]. Specifically, different from traditional charge reverse systems whose zeta potential change was always above 20 mV [41–43], the zeta potential change between pH 6.8 and 7.4 was just around 6 mV. This discrepancy was attributed to the fact that the exposed amine groups in $(Lys)_8$ would interact with the carboxyl groups in $(Glu)_8$ *via* electrostatic interaction. In other word, $(Glu)_8$ sequence was expected to embed in the $(Lys)_8$ shell and form a zipper-like structure, which limited the increase of zeta potential inevitably.

To further confirm the liberation of amine groups at mild acidic environment, fluorescence spectrum was measured when PKBE-DMA was incubated with fluorescamine at pH 6.8 and 7.4, respectively. Herein, non-fluorescence fluorescamine was employed as a sensor to detect primary amine, since it would react with primary amine to emit green fluorescence. As shown in Fig. 1C, stronger fluorescence intensity was found at pH 6.8 than that at pH 7.4. This result was consistence with the result of zeta potential change, which substantively confirmed the pH responsive liberation of amine groups. In addition, the hydrodynamic sizes of PKBE-DMA at pH 7.4 and 6.8 were comparable, which were 211.3 nm (PDI: 0.295) and 259.0 nm (PDI: 0.307), respectively (Fig. 1D). Meanwhile, PKBE-DMA showed certain stability with time prolonging at pHs of 6.8 and 7.4 (Fig. S5). TEM images revealed that PKBE-DMA could self-assemble into uniform and well dispersed spherical nanoparticles at pHs of both 6.8 (Fig. 1E) and 7.4 (Fig. 1F). Obviously, although DMA groups were detached and electrostatic attraction occurred between $(Glu)_8$ and $(Lys)_8$ at acidic environment, the self-assembly behavior would not be significantly affected.

Subsequently, HABA/Avidin assay demonstrated that around 53% biotin molecule was at the surface of chimeric peptide self-assembly, when PKBE-DMA was incubated in PBS buffer (pH 6.8) for 0.5 h. And the exposed ratio of biotin molecule dramatically decreased to around 35% at physiological pH (Fig. 1G). When PKBE-DMA was incubated in PBS for 2 h, the gap in exposed biotin molecule between pH 6.8 and 7.4 became greater, around 79% and 51% biotin was at the surface of peptide at pHs of 6.8 and 7.4, respectively. Clearly, biotin molecule was mainly steric shielded in the hydrophilic shell of PKBE-DMA self-assembly at neutrally physiological environment, which prevented the specific interaction with avidin. When PKBE-DMA was incubated at mild acidic environment, DMA was rapidly detached as proved above and the electrostatic interaction between $(Glu)_8$ and $(Lys)_8$ was recovered. The negatively charged $(Glu)_8$ would fold positively charged $(Lys)_8$. As a result, biotin underwent a position shift from the middle layer of the self-assembly to the outer layer, which was in favor of the

competitive combination with avidin. Note that some biotin molecules were also exposure at pH 7.4, since dimethylmaleic amide between Lys and DMA was very sensitive to acidity, and it could even be hydrolyzed at physiological condition to some extent. However, the hydrolysis rate at pH 6.8 is significant high than that at pH 7.4.

To further confirm that PKBE-DMA underwent a fold at mild acidity, CD spectrum at pHs of 6.8 and 7.4 was recorded. It was found that PKBE-DMA at pH 7.4 was random coil due to electrostatic repulsion among carboxyl groups in PKBE-DMA (Fig. 1H). However, at pH 6.8 for 2 h, the secondary structure of PKBE-DMA is 17% turn and 83% random coil according to Yang Reference fitting. Apparently, the random coil was due to the existence of $(Glu)_8$ and $(Lys)_8$ while the turn demonstrated the fold formation.

3.2. Tumor-selective cellular internalization of PKBE-DMA

Given that biotinylated nanoparticles could cross tumor cell membranes with ease *via* a ligand receptor-mediated process. Meanwhile, different from normal tissue, tumor tissue underwent high rate of glycolysis. The subsequent production of lactic acid led to mild acidity in tumor tissue (pH 6.3–6.9). Hence, PKBE-DMA was expected to perform a relative selectivity between normal cells and tumor cells. To confirm it, SCC-7 cell with overexpressed biotin acceptor was used as the model cell. PKE-DMA without biotin and pH insensitive PKBE-SA were used as negative controls. DLS and TEM results indicated that PKBE-DMA, PKE-DMA and PKBE-SA had similar hydrodynamic sizes (Fig. S6). Fig. S7 revealed that the fluorescences of PKBE-DMA, PKE-DMA, PKBE-SA at PBS buffer (pH 7.4) were slightly higher than that at pH 6.8. As shown in Fig. 2A1, red fluorescence signal of PKBE-DMA in SCC-7 cells at pH 6.8 was observably stronger than that at pH 7.4. For comparison, there was negligible difference in fluorescence intensity of PKBE-SA in SCC-7 cells at pHs of 6.8 and 7.4 (Fig. 2A3). Meanwhile, the fluorescence of PKBE-SA was significantly weaker than that of PKBE-DMA at pH 6.8. Apparently, the strong electrostatic repulsion between PKBE-SA

and negatively charged cell membrane restricted the cellular internalization of PKBE-SA [44]. However, for PKBE-DMA, hydrolysis of DMA under tumor acidic microenvironment was more rapidly as proved above. Both the increased zeta potential and exposed biotin may accelerate the internalization of PKBE-DMA in SCC-7 cells.

In order to get insight of the mechanism of enhanced internalization of PKBE-DMA at mild acidity, we further compared the cellular internalization between PKBE-DMA and PKE-DMA at pHs of 6.8 and 7.4. It was found that the red fluorescence intensity of PKE-DMA at pH 6.8 was just comparable to that at pH 7.4 (Fig. 2A2). Fig. S8 revealed that although DMA groups were detached at pH 6.8 and zeta potential could increase for PKE-DMA, the increment was also just around 6 mV. Clearly, this limited increment in zeta potential could not significantly improve the cellular internalization of chimeric peptide. Meanwhile, the fluorescence intensity of PKBE-DMA at pH 6.8 was remarkably stronger than that of PKE-DMA. All these results indicated that biotin-mediated internalization played a dominated role in improved cellular internalization.

Furthermore, the cellular internalization of various samples in HeLa cells (another biotin acceptor overexpressed cell-line) was also observed. As expected, similar cellular internalization tendency were observed in HeLa cells among various samples at pHs of 6.8 and 7.4 (Fig. 2B1–3), when compared with the results in SCC-7 cells. Apparently, tumor acidity-activated enhanced cellular internalization of PKBE-DMA was cell-line independent. And biotin receptor was widely existed in many tumors, which endowed PKBE-DMA with broad-spectrum tumor target ability. In addition, it was found that negligible difference in red fluorescence intensity were existed among PKBE-DMA, PKE-DMA and PKBE-SA in COS7 cells (normal cell model) at pHs of 6.8 and 7.4 (Fig. 2C1–3). And all of the fluorescence signals were weak. The average fluorescence (determined by Image J software) of various samples in SCC-7, HeLa and COS7 was also provided in Fig. S9. These results indicated that although PKBE-DMA could detach DMA group at pH 6.8 and the biotin ligand was exposed, COS7 cells had few biotin
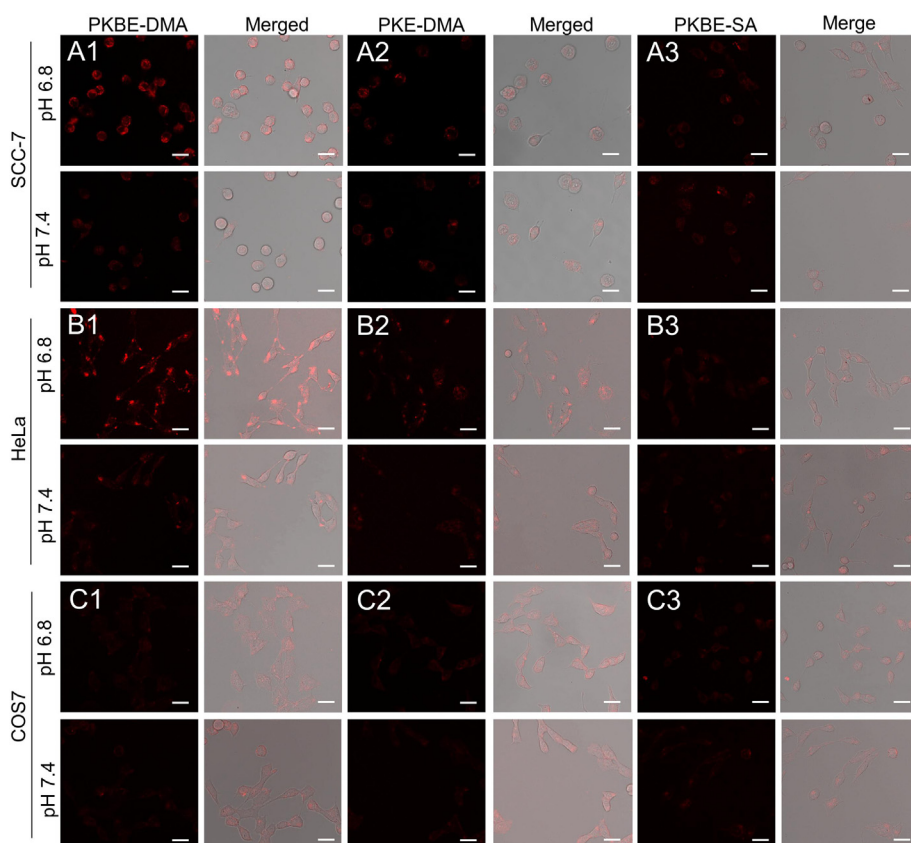
Fig. 2. Tumor specific cellular uptake. Cellular uptake of PKBE-DMA, PKE-DMA and PKBE-SA in various cell-lines at pHs of 6.8 and 7.4: (A1–A3) in SCC-7 cells; (B1–B3) in HeLa cells and (C1–C3) in COS7 cells. The samples were incubated with cells for 4 h. Red signal: PpIX. The scale bar was 20 μm. (For interpretation of the references to colour in this figure legend, the reader is referred to the web version of this article.)
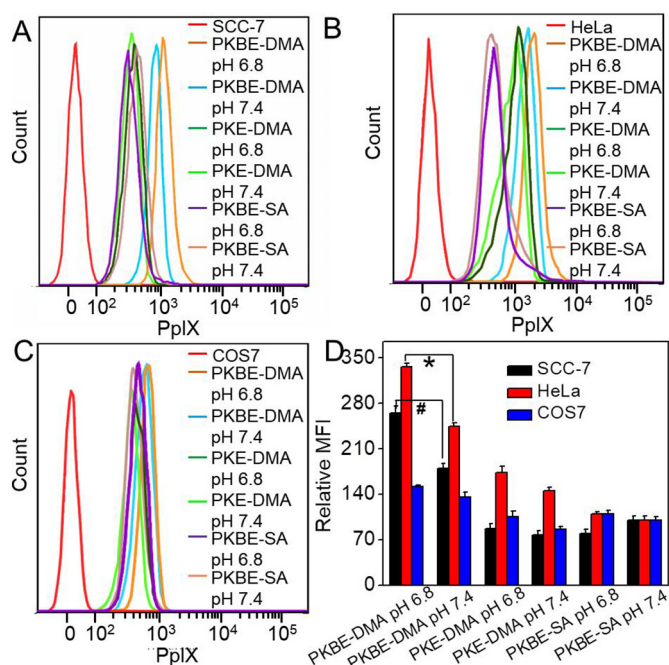
Fig. 3. Tumor specific cellular uptake. Cellular internalization of PKBE-DMA, PKE-DMA and PKBE-SA determined by flow cytometry in (A) SCC-7 cells, (B) HeLa cells, (C) COS7 cells at pHs of 6.8 and 7.4. (D) Relative MFI value of the results of flow cytometry using PKBE-SA at pH 7.4 as the standard ($*p < 0.05$; $\#p < 0.05$).

receptors, which restricted the ligand receptor-mediated cellular internalization of chimeric peptide.

Flow cytometry was used to quantitatively evaluate the cellular internalization of various samples. As show in Fig. 3A–C, PKBE-DMA exhibited significantly enhanced cellular internalization in both SCC-7 and HeLa cells at pH 6.8 than that at pH 7.4. Meanwhile, the fluorescence intensity of PKBE-DMA in both SCC-7 and HeLa cells at pH 6.8 was also higher than that of PKE-DMA and PKBE-SA. Apparently, the tendency in flow cytometry analysis was similar to that observed in CLSM. The relative mean fluorescence intensity (MFI) was also performed in Fig. 3D.

Tumor acidity-activated enhanced cellular internalization of PKBE-DMA in tumor cells was also evaluated *via* MTT assay. Fig. S10 indicated that PKBE-DMA, PKE-DMA and PKBE-SA had negligible dark toxicity, since photo irradiation was vital for PDT. During PDT, photosensitizers absorbed light and then transferred energy to surrounding tissue oxygen, so that generated ROS could make irreversible damage to tumor cells [10]. As shown in Fig. 4A and B, PKBE-DMA exhibited significantly higher toxicity at pH 6.8 than that at pH 7.4 in both SCC-7 and HeLa cells. In contrast, the toxicity difference between pH 6.8 and 7.4 in these two cells significantly decreased for both PKE-DMA and PKBE-SA (Fig. 4A and B). Meanwhile, both the cytotoxicity of PKE-DMA and PKBE-SA was lower than that of PKBE-DMA at pH 6.8. These results were consistence to that of cellular internalization observed *via* CLSM and flow cytometry, indicating that tumor acidity-activated biotin exposure could enhance the photodynamic therapeutic efficacy. For comparison, PKBE-DMA, PKE-DMA and PKBE-SA performed similar toxicity in COS7 cells (Fig. 4C). Note that the cytotoxicity in HeLa cells was greater than that in SCC-7 cells under the same condition, since the cellular internalization ability of therapeutic agent was cell-line dependent.

### 3.3. Tumor targeted fluorescence imaging and in vivo biodistribution

Having confirmed the tumor selectivity of PKBE-DMA *in vitro*, the
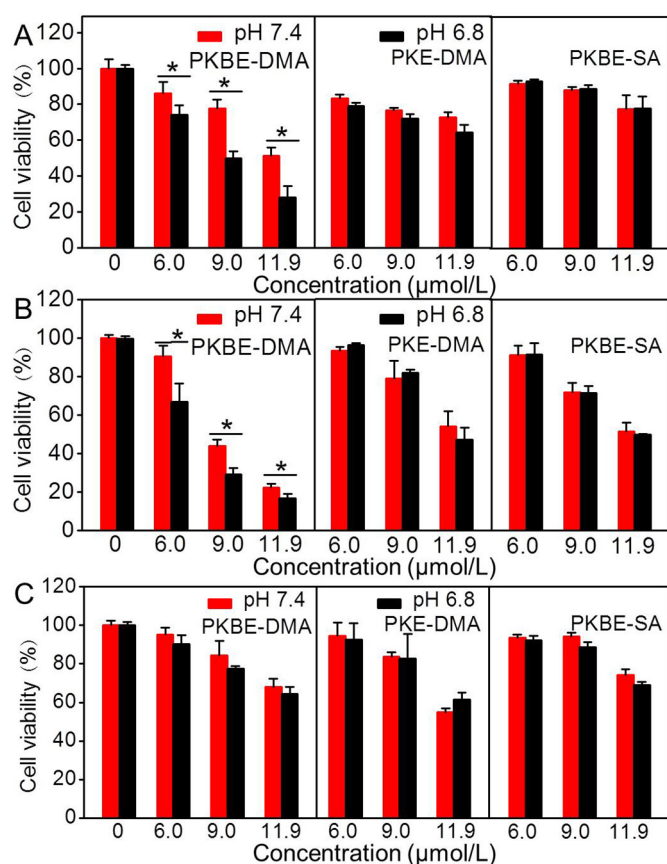
Fig. 4. Tumor cell specific damage. *In vitro* cytotoxicity of PKBE-DMA, PKE-DMA and PKBE-SA in various cell-lines at pHs of 6.8 and 7.4: (A) in SCC-7 cells ($*p < 0.05$); (B) in HeLa cells and (C) in COS7 cells.

feasibility of PKBE-DMA in tumor targeted accumulation *in vivo* was investigated *via* a small animal fluorescence imaging system. DLS results indicated that PKBE-DMA, PKE-DMA and PKBE-SA exhibited well stability in serum, suggesting the great *in vivo* potential (Fig. S11) [45–47]. As shown in Fig. 5A, the fluorescence signal of PKBE-DMA in tumor region gradually increased after tail intravenous injection. And it reached the peak value at the 5th h, suggesting the efficient accumulation of PKBE-DMA in tumor. Then although fluorescence signal gradually decreased inevitably due to the metabolism, bright fluorescence signal could be still observed at the 9th h. For comparison, moderate fluorescence signal of PKE-DMA could be observed only before 3 h post *in vivo* injection due to the EPR effect. Thereafter, the signal dramatically decreased. The fluorescence at the 7th h was nearly undetectable. Obviously, PKBE-DMA could accumulate in tumor region more efficiently than PKE-DMA. This result substantially demonstrated that tumor acidity-activated biotin exposure could accelerate cellular internalization as well as enhance tumor specific accumulation efficiently. In addition, the fluorescence signal in tumor in PKBE-SA group was also weak, which was even slightly weaker than that of PKE-DMA group, indicating that the DMA detachment-induced zeta potential increment could enhance tumor accumulation to some extent.

At 24 h post *in vivo* injection, tumor and organs were exfoliated and imaged. As shown in Fig. 5B, the fluorescence signals of PKBE-DMA, PKE-DMA and PKBE-SA in liver or kidney were comparable. Meanwhile, PKBE-DMA group had the greatest fluorescence signal in tumor region, which was even stronger than that in the main metabolic organ liver and kidney, revealing the high efficient tumor accumulation of PKBE-DMA. The quantitatively relative MFI value was also provided in Fig. 5C. Relative MFI value of PKBE-DMA in tumor was around 1.3 and 1.9-fold to that of PKE-DMA and PKBE-SA in tumor, respectively.
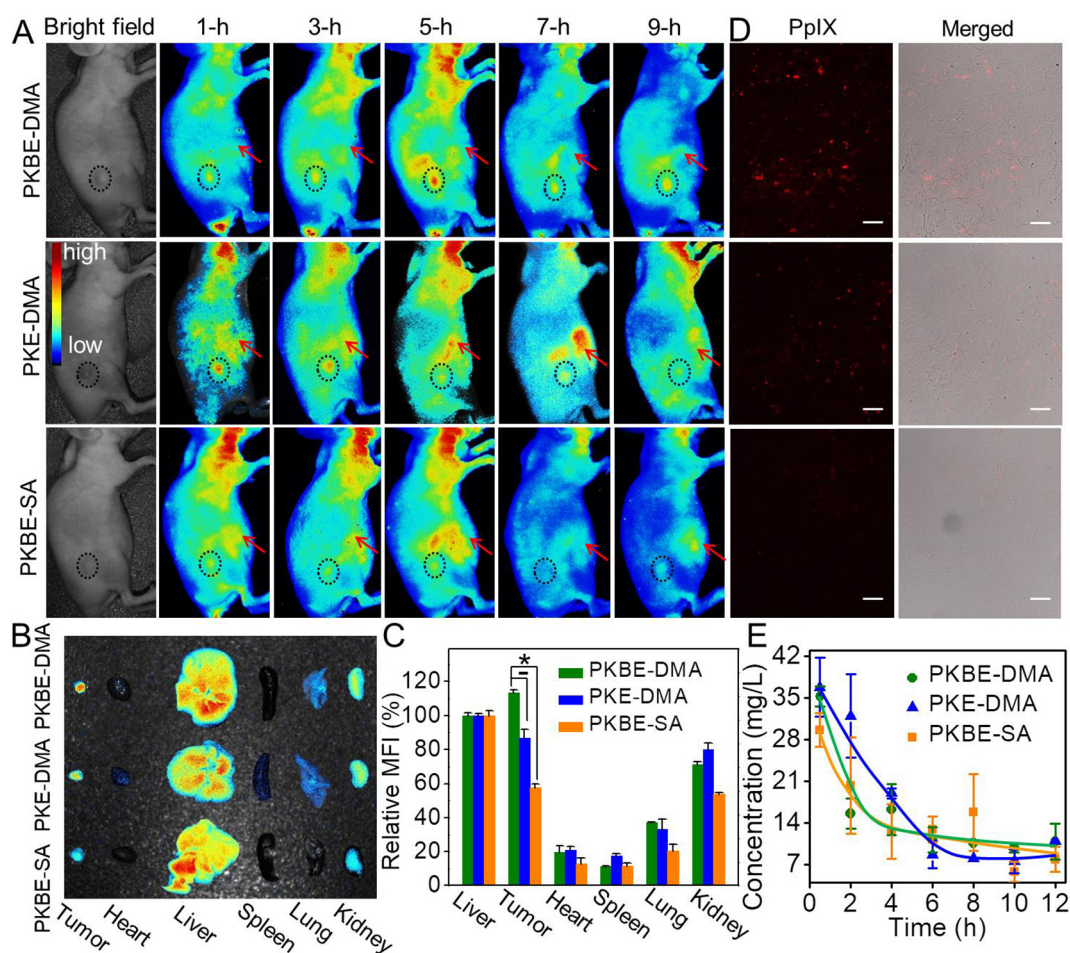
Fig. 5. *In vivo* imaging and pharmacokinetics. *In vivo* biodistribution of various samples: (A) the fluorescence of PKBE-DMA, PKE-DMA and PKBE-SA at different time points after vein injection, the red arrow pointed to liver region and the tumor tissue was in the dark circle; (B) fluorescence imaging of PKBE-DMA, PKE-DMA and PKBE-SA in tumor and various organs at 24 h post *in vivo* injection; (C) the quantitative analysis of the fluorescence intensity of various samples at 24 h post injection (*p, ⁻p < 0.05). MFI value in liver was used as the standard (100%). (D) The fluorescence of PKBE-DMA, PKE-DMA and PKBE-SA in tumor tissue. The scale bar was 50 μm. (E) The blood retention kinetic of PKBE-DMA, PKE-DMA and PKBE-SA after intravenous injection. Each group had 4 mice. (For interpretation of the references to colour in this figure legend, the reader is referred to the web version of this article.)

Furthermore, the tumor frozen sections samples were obtained and the fluorescence of PKBE-DMA, PKE-DMA and PKBE-SA in tumor tissue was observed *via* CLSM. It was found that the fluorescence intensity of PKBE-DMA in tumor was significantly stronger than that of PKE-DMA and PKBE-SA (Fig. 5D). Obviously, the tendency observed *via* CLSM was highly consistent with that observed *via* a small animal imaging system, which substantially demonstrated the tumor enhanced accumulation of PKBE-DMA *in vivo*. Pharmacokinetic study in Fig. 5E showed that there did not exist great discrepancy in blood retention among PKBE-DMA, PKE-DMA and PKBE-SA, suggesting the enhanced tumor accumulation of PKBE-DMA was mainly due to the acidity-triggered biotin exposure. Meanwhile, the CMC values of PKBE-DMA at pHs of 6.8 and 7.4 were 3.4 mg/L and 12.6 mg/L, respectively, which ensured the micellar structure *in vivo* (Fig. S12).

3.4. In vivo tumor targeted photodynamic therapy and side effects evaluation

To confirm that PKBE-DMA could show tumor specific and efficient inhibition, *in vivo* antitumor effect was investigated using SCC-7 tumor-bearing nude mouse as the animal model. As shown in Fig. 6A, although the tumor volume in both PKE-DMA and PKBE-SA groups with light irradiation was smaller than PBS group, it still quickly became bigger with prolonging of the feeding time. In sharp contrast, PKBE-DMA with

light irradiation dramatically inhibited tumor growth. This observable tumor inhibition was due to the enhanced tumor accumulation and internalization of chimeric peptide in tumor region. After the treatment was finished, all tumors were collected, imaged and weighed. Fig. 6B revealed that tumors in PKBE-DMA group with light irradiation were the smallest, when compared with other groups. And the average tumor weight gradually decreased in the following order: PBS group > PKBE-DMA group without light irradiation > PKBE-SA group with light irradiation > PKE-DMA group with light irradiation ≫ PKBE-DMA group with light irradiation (Fig. 6C). Clearly, the tendency was highly consistence to that of tumor volume. Furthermore, the physiological morphology in tumor tissues was observed *via* H&E staining. As shown in Fig. 6D, the cell densities in tumor tissue in PKBE-SA and PKE-DMA groups with light irradiation were decreased to some extent, when compared with PBS group. Meanwhile, PKBE-DMA group with light irradiation presented greatest nuclei absence. All these results substantially demonstrated that PKBE-DMA presented most efficient PDT efficacy in biotin receptor overexpressed acidic tumor tissue.

Considering that PKBE-DMA presented well tumor targeting ability and PDT was a local therapy, PKBE-DMA with light irradiation was anticipated to show minimal *in vivo* side effects. To confirm it, body weight of mice was recorded during treatment. As expected, negligible weight fluctuates were observed in all groups during PDT (Fig. S13), suggesting the well biosafety of PKBE-DMA. To get insight of the
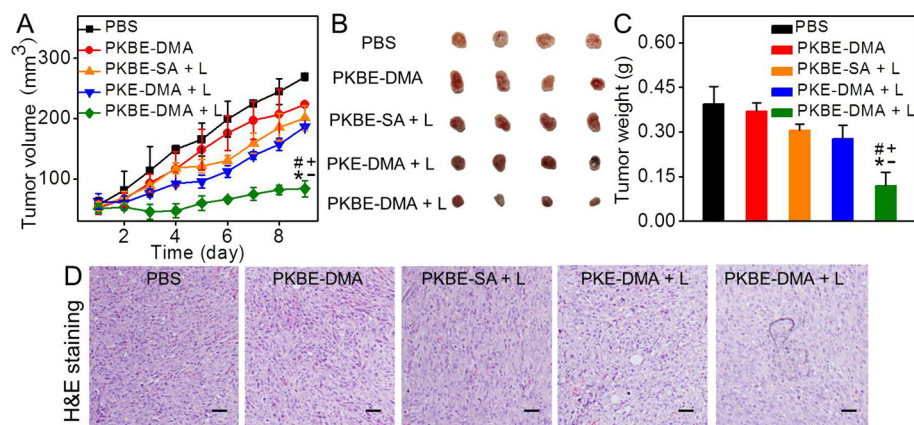
Fig. 6. *In vivo* antitumor effect. (A) Average tumor volume; (B) tumor images and (C) average tumor weight in various groups. PpIX was 3 mg/kg mouse body weight and the irradiation time was 10 min. Each group had 4 mice. $^{\#}p$, ^{+}p, $^{*}p$ and $^{-}p < 0.05$, when the PKBE-DMA with light irradiation group was compared with the groups of PBS, PKBE-DMA, PKBE-SA with light irradiation, and PKE-DMA with light irradiation. (D) H&E staining of tumors in various groups. The scale bar was 50 μm. "L" means light irradiation.
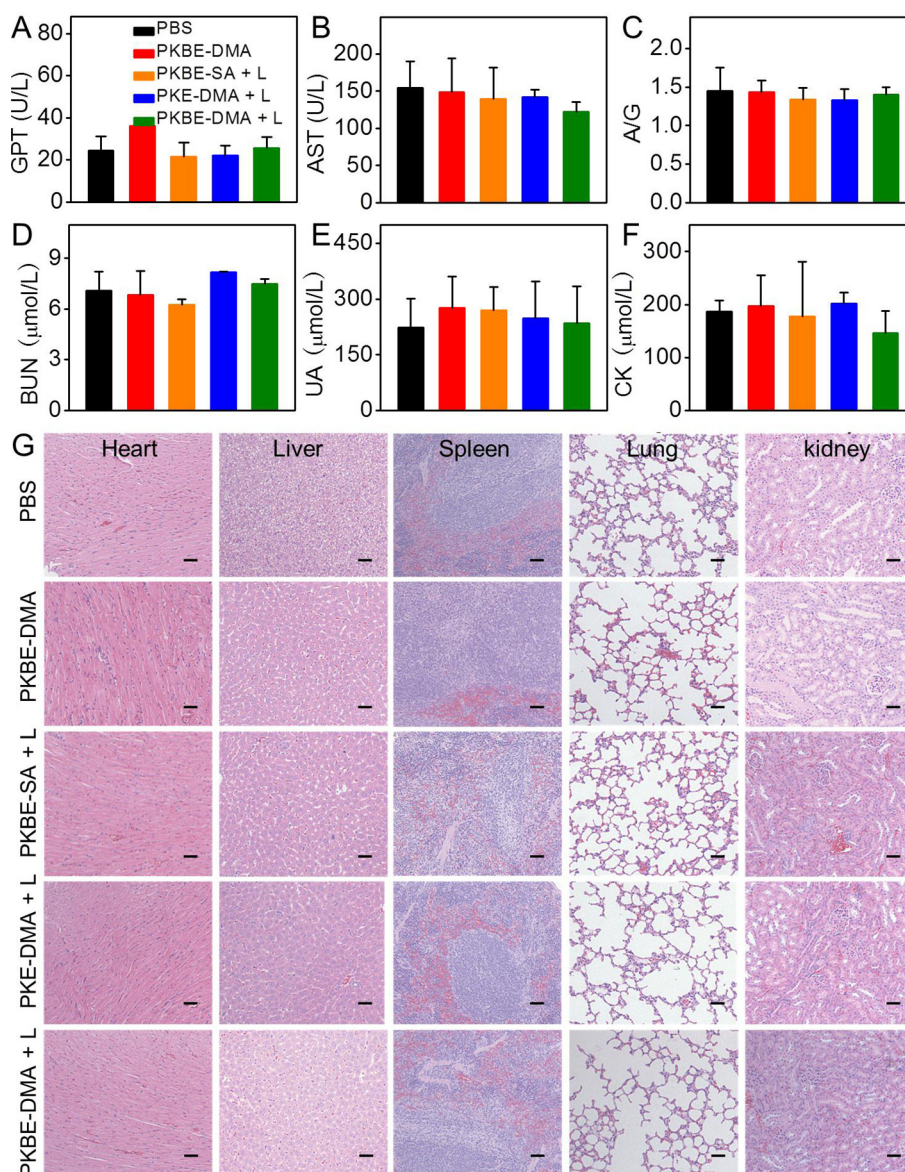
Fig. 7. *In vivo* systemic toxicity evaluation. Serum biochemical indexes in terms of (A) GPT; (B) AST; (C) A/G; (D) BUN; (E) UA and (F) CK. (G) Physiological morphology observation of various tissues including heart, liver, spleen, lung and kidney *via* H&E staining. Each group had 4 mice. The scale bar was 50 μm. "L" means light irradiation.

potential systemic toxicity of PKBE-DMA under light irradiation, various physiological indexes were measured *via* blood routine analysis in terms of liver, kidneys and heart. It was found that the expression levels in various groups in terms of the liver function markers including glutamic pyruvate transaminase (GPT, Fig. 7A), aspartate aminotransferase (AST, Fig. 7B) and A/G (Fig. 7C), kidney function markers including blood urea nitrogen (BUN, Fig. 7D) and uric acid (UA, Fig. 7E) and heart function marker including creatine kinase (CK, Fig. 7F) were all in normal range, when compared with PBS control group and previous reports [48,49]. These results demonstrated that PKBE-DMA during PDT would not induce liver, kidneys and heart damage. The negligible systemic toxicity was further evaluated by the physiological morphology observation through H&E staining. As shown in Fig. 7G, the tissue morphologies including heart, liver, spleen, lung and kidneys in various groups were normal. Obviously, PKBE-DMA during PDT performed well antitumor effect with minimal side effects, since ROS had an instantaneous lifetime (< 40 ns) and a short action range (around 20 nm) [50,51], the well tumor accumulation of PKBE-DMA restricted ROS damage in the tumor region furthest during PDT.

4. Conclusions

In summary, we designed a steric shielding protected chimeric peptide PKBE-DMA for tumor acidic environment activated enhanced photodynamic therapy. At physiological environment, biotin molecule could be efficiently shielded in hydrophilic shell of PKBE-DMA self-assembly. Once arriving at tumor acidic environment, DMA group was detached. The electrostatic attraction mediated the formation of zipper-like fold between $(Lys)_8$ and $(Glu)_8$ as well as the pop-up of biotin. The exposed biotin accelerated the specific accumulation and acceleration of chimeric peptide in tumor, which realized enhanced photodynamic therapy with negligible side effects. This shielding/deshielding strategy demonstrated here did not require external stimuli and possess the broad-spectrum targeting ability, which should show great potential for tumor therapy.

Acknowledgements

Competing financial interests

The authors declare no competing financial interests.

Appendix A. Supplementary data

Supplementary data to this article can be found online at https://doi.org/10.1016/j.jconrel.2018.04.033.

References

[1] A.N. Zelikin, C. Ehrhardt, A.M. Healy, Materials and methods for delivery of biological drugs, Nat. Chem. 8 (2016) 997–1007.

[2] W. Jiang, C.A. von Roemeling, Y.X. Chen, Y.Q. Qie, X.J. Liu, J.Z. Chen, B.Y.S. Kim, Designing nanomedicine for immuno-oncology, Nat. Biomed. Eng. 1 (2017) 0029–0040.

[3] J.N. Tang, D.L. Shen, T.G. Caranasos, Z.G. Wang, A.C. Vandergriff, T.A. Allen, M.T. Hensley, P.-U. Dinh, J. Cores, T.S. Li, J.Y. Zhang, Q.C. Kan, K. Cheng, Therapeutic microparticles functionalized with biomimetic cardiac stem cell membranes and secretome, Nat. Commun. 8 (2017) 13724–13733.

[4] C.E. Callmann, C.V. Barback, M.P. Thompson, D.J. Hall, R.F. Mattrey, N.C. Gianneschi, Therapeutic enzyme-responsive nanoparticles for targeted delivery and accumulation in tumors, Adv. Mater. 27 (2015) 4611–4615.

[5] S. Mitra, H.S. Sasmal, T. Kundu, S. Kandambeth, K. Illath, D.D. Díaz, R. Banerjee, Targeted drug delivery in covalent organic nanosheets (CONs) *via* sequential

[6] H. Chen, L. Xiao, Y. Anraku, P. Mi, X. Liu, H. Cabral, A. Inoue, T. Nomoto, A. Kishimura, N. Nishiyama, K. Kataoka, Polyion complex vesicles for photoinduced intracellular delivery of amphiphilic photosensitizer, J. Am. Chem. Soc. 136 (2014) 157–163.

[7] Y. Lu, A.A. Aimetti, R. Langer, Z. Gu, Bioresponsive materials, Nat. Rev. Mater. 2 (2016) 16075–16092.

[8] S.B. Ruan, C. Hu, X. Tang, X.L. Cun, W. Xiao, K.R. Shi, Q. He, H.L. Gao, Increased gold nanoparticle retention in brain tumors by *in situ* enzyme-induced aggregation, ACS Nano 10 (2016) 10086–10098.

[9] P. Kulkarni, M.K. Haldar, S. You, Y. Choi, S. Mallik, Hypoxia-responsive polymer-somes for drug delivery to hypoxic pancreatic cancer cells, Biomacromolecules 17 (2016) 2507–2513.

[10] K. Han, J. Zhang, W.Y. Zhang, S.B. Wang, L.M. Xu, C. Zhang, X.Z. Zhang, H.Y. Han, Tumor-triggered geometrical shape switch of chimeric peptide for enhanced *in vivo* tumor internalization and photodynamic therapy, ACS Nano 11 (2017) 3178–3188.

[11] H.C. Yen, H. Cabral, P. Mi, K. Toh, Y. Matsumoto, X. Liu, H. Koori, A. Kim, K. Miyazaki, Y. Miura, N. Nishiyama, K. Kataoka, Light-induced cytosolic activation of reduction-sensitive camptothecin-loaded polymeric micelles for spatiotemporally controlled *in vivo* chemotherapy, ACS Nano 8 (2014) 11591–11602.

[12] T. Nomoto, S. Fukushima, M. Kumagai, K. Miyazaki, A. Inoue, P. Mi, Y. Maeda, K. Toh, Y. Matsumoto, Y. Morimoto, A. Kishimura, N. Nishiyama, K. Kataoka, Calcium phosphate-based organic–inorganic hybrid nanocarriers with pH-responsive on/off switch for photodynamic therapy, Biomater. Sci. 4 (2016) 826–838.

[13] R.V.J. Chari, M.L. Miller, W.C. Widdison, Antibody-drug conjugates: an emerging concept in cancer therapy, Angew. Chem. Int. Ed. 53 (2014) 3796–3827.

[14] S. Kunjachan, R. Pola, F. Gremse, B. Theek, J. Ehling, D. Moeckel, B. Hermanns-Sachweh, M. Pechar, K. Ulbrich, W.E. Hennink, G. Storm, W. Lederle, F. Kiessling, T. Lammers, Passive *vs.* active tumor targeting using RGD-and NGR-modified polymeric nanomedicines, Nano Lett. 14 (2014) 972–981.

[15] J. Zhang, Z.F. Yuan, Y. Wang, W.H. Chen, G.F. Luo, S.X. Cheng, R.X. Zhuo, X.Z. Zhang, Multifunctional envelope-type mesoporous silica nanoparticles for tumor-triggered targeting drug delivery, J. Am. Chem. Soc. 135 (2013) 5068–5073.

[16] H.N. He, L. Sun, J.X. Ye, E.G. Liu, S.H. Chen, Q.L. Liang, M.C. Shin, V.C. Yang, Enzyme-triggered, cell penetrating peptide-mediated delivery of anti-tumor agents, J. Control. Release 240 (2016) 67–76.

[17] Z.F. Yuan, D. Zhao, X.Q. Yi, R.X. Zhuo, F. Li, Steric protected and illumination-activated tumor targeting accessory for endowing drug-delivery systems with tumor selectivity, Adv. Funct. Mater. 24 (2014) 1799–1807.

[18] L. Zhu, P. Kate, V.P. Torchilin, Matrix metalloprotease 2-responsive multifunctional liposomal nanocarrier for enhanced tumor targeting, ACS Nano 6 (2012) 3491–3498.

[19] E.L. Jin, B. Zhang, X.R. Sun, Z.X. Zhou, X.P. Ma, Q.H. Sun, J.B. Tang, Y.Q. Shen, E.V. Kirk, W.J. Murdoch, M. Radosz, Acid-active cell-penetrating peptides for *in vivo* tumor-targeted drug delivery, J. Am. Chem. Soc. 135 (2013) 933–940.

[20] S. Pilon-Thomas, K.N. Kodumudi, A.E. El-Kenawi, S. Russell, A.M. Weber, K. Luddy, M. Damaghi, J.W. Wojtkowiak, J.J. Mulé, A. Ibrahim-Hashim, R.J. Gillies, Neutralization of tumor acidity improves antitumor responses to immunotherapy, Cancer Res. 76 (2016) 1381–1390.

[21] V.A. Sethuraman1, Y.H. Bae, TAT peptide-based micelle system for potential active targeting of anti-cancer agents to acidic solid tumors, J. Control. Release 118 (2007) 216–224.

[22] E.S. Lee, Z.G. Gao, D. Kim, K. Park, I.C. Kwon, Y.H. Bae, Super pH-sensitive multifunctional polymeric micelle for tumor pHe specific TAT exposure and multidrug resistance, J. Control. Release 129 (2008) 228–236.

[23] Y. Lee, T. Ishii, H. Cabral, H.J. Kim, J.H. Seo, N. Nishiyama, H. Oshima, K. Osada, K. Kataoka, Charge-conversional polyionic complex micelles-efficient nanocarriers for protein delivery into cytoplasm, Angew. Chem. Int. Ed. 48 (2009) 5309–5312.

[24] Y. Lee, S. Fukushima, Y. Bae, S. Hiki, T. Ishii, K. Kataoka, A protein nanocarrier from charge-conversion polymer in response to endosomal pH, J. Am. Chem. Soc. 129 (2007) 5362–5363.

[25] Y. Lee, K. Miyata, M. Oba, T. Ishii, S. Fukushima, M. Han, H. Koyama, N. Nishiyama, K. Kataoka, Charge-conversion ternary polyplex with endosome disruption moiety: a technique for efficient and safe gene delivery, Angew. Chem. Int. Ed. 47 (2008) 5163–5166.

[26] J.Z. Du, T.M. Sun, W.J. Song, J. Wu, J. Wang, A tumor-acidity-activated charge-conversional nanogel as an intelligent vehicle for promoted tumoral-cell uptake and drug delivery, Angew. Chem. Int. Ed. 49 (2010) 3621–3626.

[27] J.Z. Du, C.Q. Mao, Y.Y. Yuan, X.Z. Yang, J. Wang, Tumor extracellular acidity-activated nanoparticles as drug delivery systems for enhanced cancer therapy, Biotechnol. Adv. 32 (2014) 789–803.

[28] J.Z. Du, X.J. Du, C.Q. Mao, J. Wang, Tailor-made dual pH-sensitive polymer-dox-orubicin nanoparticles for efficient anticancer drug delivery, J. Am. Chem. Soc. 133 (2011) 17560–17563.

[29] H. Cheng, J.Y. Zhu, X.D. Xu, W.X. Qiu, Q. Lei, K. Han, Y.J. Cheng, X.Z. Zhang, Activable cell-penetrating peptide conjugated prodrug for tumor targeted drug delivery, ACS Appl. Mater. Interfaces 7 (2015) 16061–16069.

[30] R. Weinstain, E.N. Savariar, C.N. Felsen, R.Y. Tsien, *In vivo* targeting of hydrogen peroxide by activatable cell-penetrating peptides, J. Am. Chem. Soc. 136 (2014) 874–877.

[31] K. Han, S.B. Wang, Q. Lei, J.Y. Zhu, X.Z. Zhang, Ratiometric biosensor for aggregation-induced emission-guided precise photodynamic therapy, ACS Nano 9 (2015) 10268–10277.

[32] K. Han, Q. Lei, H.Z. Jia, S.B. Wang, W.N. Yin, W.H. Chen, S.X. Cheng, X.Z. Zhang, A tumor targeted chimeric peptide for synergistic endosomal escape and therapy by dual-stage light manipulation, Adv. Funct. Mater. 25 (2015) 1248–1257.

[33] S.Y. Li, W.X. Qiu, H. Cheng, F. Gao, F.Y. Cao, X.Z. Zhang, A versatile plasma membrane engineered cell vehicle for contact-cell-enhanced photodynamic therapy, Adv. Funct. Mater. 27 (2017) 1604916–1604927.

[34] K. Han, Q. Lei, S.B. Wang, J.J. Hu, W.X. Qiu, J.Y. Zhu, W.N. Yin, X. Luo, X.Z. Zhang, Dual-stage-light-guided tumor inhibition by mitochondria-targeted photodynamic therapy, Adv. Funct. Mater. 25 (2015) 2961–2971.

[35] S.R. Bobe, M. Al Kobaisi, S.V. Bhosale, S.V. Bhosale, Solvent-tuned self-assembled nanostructures of chiral l/d-phenylalanine derivatives of protoporphyrin IX, ChemistryOpen 4 (2015) 516–522.

[36] S.V. Bhosale, M.B. Kalyankar, S.V. Bhosale, S.G. Patil, C.H. Lalander, S.J. Langford, S.V. Nalage, Supramolecular self-assembly of protoporphyrin IX amphiphiles into worm-like and particular aggregates, Supramol. Chem. 23 (2011) 263–268.

[37] L.Y. Cui, Q.Y. Lin, C.S. Jin, W.L. Jiang, H. Huang, L.L. Ding, N. Muhanna, J.C. Irish, F. Wang, J. Chen, G. Zheng, A PEGylation-free biomimetic porphyrin nanoplatform for personalized cancer theranostics, ACS Nano 9 (2015) 4484–4495.

[38] G. Zheng, Porphysome nanotechnology for image-guided phototherapy, Photodiagn. Photodyn. Ther. 17 (2017) A33.

[39] K.K. Ng, G. Zheng, Molecular interactions in organic nanoparticles for photo-theranostic applications, Chem. Rev. 115 (2015) 11012–11042.

[40] T. Feng, X.Z. Ai, G.H. An, P.P. Yang, Y.L. Zhao, Charge-convertible carbon dots for imaging-guided drug delivery with enhanced *in vivo* cancer therapeutic efficiency, ACS Nano 10 (2016) 4410–4420.

[41] C.Y. Sun, S. Shen, C.F. Xu, H.J. Li, Y. Liu, Z.T. Cao, X.Z. Yang, J.X. Xia, J. Wang, Tumor acidity-sensitive polymeric vector for active targeted siRNA delivery, J. Am. Chem. Soc. 137 (2015) 15217–15224.

[42] K. Han, W.Y. Zhang, J. Zhang, Q. Lei, S.B. Wang, J.W. Liu, X.Z. Zhang, H.Y. Han, Acidity-triggered tumor-targeted chimeric peptide for enhanced intra-nuclear photodynamic therapy, Adv. Funct. Mater. 26 (2016) 4351–4361.

[43] H.J. Li, J.Z. Du, J. Liu, X.J. Du, S. Shen, Y.H. Zhu, X.Y. Wang, X.D. Ye, S.M. Nie, J. Wang, Smart superstructures with ultrahigh pH-sensitivity for targeting acidic tumor microenvironment: instantaneous size switching and improved tumor penetration, ACS Nano 10 (2016) 6753–6761.

[44] M.J. Sun, J. Li, C.T. Zhang, Y. Xie, H.Z. Qiao, Z.G. Su, D. Oupický, Q.N. Ping, Arginine-modified nanostructured lipid carriers with charge-reversal and pH-sensitive membranolytic properties for anticancer drug delivery, Adv. Healthc. Mater. 6 (2017) 1600693–1600705.

[45] W.B. Hu, T.C. He, R.C. Jiang, J. Yin, L. Li, X.M. Lu, H. Zhao, L. Zhang, L. Huang, H.D. Sun, W. Huang, Q.L. Fan, Inner salt-shaped small molecular photosensitizer with extremely enhanced two-photon absorption for mitochondrial-targeted photodynamic therapy, Chem. Commun. 53 (2017) 1680–1683.

[46] W.B. Hu, H.H. Ma, B. Hou, H. Zhao, Y. Ji, R.C. Jiang, X.M. Hu, X.M. Lu, L. Zhang, Y.F. Tang, Q.L. Fan, W. Huang, Engineering lysosome-targeting BODIPY nanoparticles for photoacoustic imaging and photodynamic therapy under near-infrared light, ACS Appl. Mater. Interfaces 8 (2016) 12039–12047.

[47] R.P. Zhang, Q.L. Fan, M. Yang, K. Cheng, X.M. Lu, L. Zhang, W. Huang, Z. Cheng, Engineering melanin nanoparticles as an efficient drug-delivery system for imaging-guided chemotherapy, Adv. Mater. 27 (2015) 5063–5069.

[48] L. Yang, H.L. Kuang, W.Y. Zhang, Z.P. Aguilar, Y.H. Xiong, W.H. Lai, H.Y. Xu, H. Wei, Size dependent biodistribution and toxicokinetics of iron oxide magnetic nanoparticles in mice, Nanoscale 7 (2015) 625–636.

[49] J.X. Wang, G.Q. Zhou, C.Y. Chen, H.W. Yu, T.C. Wang, Y.M. Ma, G. Jia, Y.X. Gao, B. Li, J. Sun, Y.F. Li, F. Jiao, Y.L. Zhao, Z.F. Chai, Acute toxicity and biodistribution of different sized titanium dioxide particles in mice after oral administration, Toxicol. Lett. 168 (2007) 176–185.

[50] M. Rajendran, Quinones as photosensitizer for photodynamic therapy: ROS generation, mechanism and detection methods, Photodiagn. Photodyn. Ther. 13 (2016) 175–187.

[51] Y.J. Chung, B.I. Lee, J.W. Ko, C.B. Park, Photoactive g-C_3N_4 nanosheets for light-induced suppression of alzheimer's β-amyloid aggregation and toxicity, Adv. Healthc. Mater. 5 (2016) 1560–1565.